The Microbead: A 0.009 mm³ Implantable Wireless Neural Stimulator

Adam Khalifa , *Student Member, IEEE*, Yuxin Liu, Yasha Karimi , *Student Member, IEEE*, Qihong Wang, Adebayo Eisape, Milutin Stanaćević , *Member, IEEE*, Nitish Thakor, *Fellow, IEEE*, Zhenan Bao , and Ralph Etienne-Cummings , *Fellow, IEEE*

Abstract—**Wirelessly powered implants are increasingly being developed to interface with neurons in the brain. They often rely on microelectrode arrays, which are limited by their ability to cover large cortical surface areas and long-term stability because of their physical size and rigid configuration. Yet some clinical and research applications prioritize a distributed neural interface over one that offers high channel count. One solution to make large scale, fully specifiable, electrical stimulation/recording possible, is to disconnect the electrodes from the base, so that they can be arbitrarily placed freely in the nervous system. In this work, a wirelessly powered stimulating implant is miniaturized using a novel electrode integration technique, and its implanted depth maximized using new optimization design methods for the transmitter and receiver coils. The stimulating device is implemented in a 130 nm CMOS technology with the following characteristics: 300 μm $\times$ 300 μm $\times$ 80 μm size; optimized two-coil inductive link; and integrated circuit, electrodes and coil. The wireless and stimulation capability of the implant is demonstrated in a conductive medium, as well as in-vivo. To the best of our knowledge, the fabricated free-floating miniaturized implant has the best depth-to-volume ratio making it an excellent tool for minimally-invasive distributed neural interface, and thus could eventually complement or replace the rigid arrays that are currently the state-of-the-art in brain set-ups.**

Index Terms—**Free-floating implant, miniaturization, microelectrode design, neural stimulation, wireless power transfer.**

I. INTRODUCTION

THE demand for wirelessly powered implantable medical devices (IMDs) [1]–[4] is rapidly growing as they do not require batteries, which necessitates periodic surgeries to carry out their replacement, and eliminates the need of percutaneous wired connections to implanted electrodes, which can cause infections. Remotely-powered IMDs that enable safer and smaller neural interfaces are especially useful to freely moving animals and human subjects. Even more so for chronic applications, since rigid tethered electrodes suffer from micromotion, which results in tissue inflammation and scar formation around the electrodes [5]–[8].

Most of the fabricated wirelessly-powered implantable medical devices (IMDs) rely on microelectrode arrays (MEAs) to interface with neurons in the central nervous system (CNS) [1]–[3], [9], [10]. Unfortunately, MEAs such as the Utah array, share significant shortcomings, the biggest being the strict limit on recording/stimulation configuration and location. MEAs offer high channel count, but localized coverage of the cerebral cortex, thus a single MEA cannot be used to record/stimulate multiple regions. If the freedom to choose between different depths is not needed then multiple MEAs could be used instead of one, but would result in very invasive surgical procedures. Regarding applications involving large mammals (including humans) with folded cortices, MEAs are not easily inserted between the folds and ridges of the brain surface. Furthermore, if the MEA is integrated into a wirelessly powered implant and made small enough to successfully be placed between the folds of the cortex, then a large rotational misalignment would occur, leading to a significant decrease in power transfer efficiency.

The removal of the centralized and anchored MEA base results in free-floating electrodes that substantially increase the anatomical sites for recording/stimulation. These single-channel implants trade lower channel count for more cortical coverage, and can thus be placed right next to the targeted volume of cortical cells, allowing clinicians and researchers to be more specific in their treatments or experiments. Some of the brain interfacing applications prioritize a distributed neural interface over one that offers a high channel count. Examples include: i) revolutionizing our understanding of the brain by studying the correlations between neural networks from different regions of the brain and the mechanisms of cognitive functions [11], [12]; ii) understanding and treating neurological disorders that affect distributed locations throughout the CNS [13]; and iii) covering a larger area in the sensorimotor cortex of amputees to more accurately control robotic prosthetic limbs [14] or better evoke a sense of touch [15].
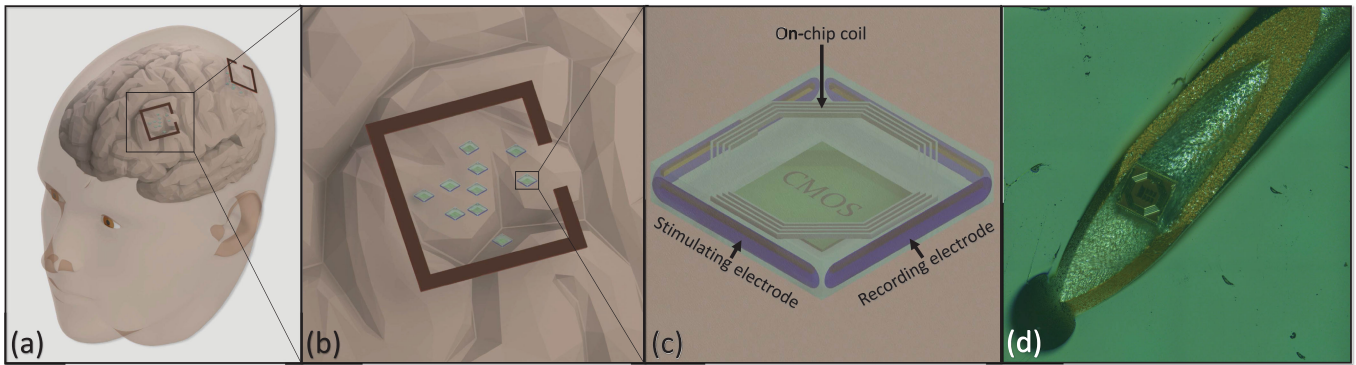
Fig. 1. A 3D drawing of (a) scattered microbeads in the cerebral cortex, (b) a close up view of the Tx coil, and (c) a close up view of the planned packaged wirelessly powered microbead with two electrodes for stimulation and two for recording. (d) A micrograph of the microbead, which can be entirely implanted into the brain by means of a syringe with a 22G needle.

The spinal cord and the peripheral nervous system (PNS), especially mixed nerves that contain both sensory and motor fibers, could also benefit from a distributed neural interface. A good example is the multi-selective stimulation of sciatic nerves that can help paralyzed people to have balanced standing and efficient walking [16]. Even a single wireless ultra-small IMD that can be placed directly at the site of stimulation/recording could be very useful to some clinical applications. For instance, selectively localizing and stimulating specific fibers inside a nerve bundle can eliminate side effects caused by the inadvertent stimulation of adjacent fibers [17], [18].

Some researchers have demonstrated wirelessly-powered single-channel stimulating IMDs [19]–[26] that have the potential to be scattered throughout the CNS and PNS. However, they are currently bulky (>0.4 mm^3) and thus too invasive as a great number of IMDs need to be surgically implanted into a dense brain or a small nerve bundle. They demonstrate tremendous progress in developing a new generation of instrumented micro-electrode, but require further miniaturization in order to truly become practical in the neuroscience and neuro-prosthetic field. Continued miniaturization would allow: i) more of these floating IMDs to be inserted into the brain, ii) more precision when targeting specific brain regions or nerve fibers, iii) compatibility with minimally invasive implantation procedures, and iv) a reduction in the body's foreign response [27], [28]. Unfortunately, the volume of the ASIC and off-chip components, and the wireless link efficiency limit the extent of implant miniaturization, and thus innovative design methods are needed to address these challenges.

To address the need for a smaller distributed free-floating neural interface, we propose the "microbead" (Fig. 1). The ultra-compact neural implant includes everything it needs (electrodes, coil, circuitry) on a single silicon chip. The vision of this work is to be able to implant hundreds of microbeads in the CNS, providing a revolutionary neural interfacing tool for neuroscientists and clinicians. To alleviate the surgical challenges currently faced while implanting MEAs or electrocorticography electrodes (removal of skin, bone, and meninges and repositioning them back), the microbead is miniaturized to enable direct injection into the target brain region via a syringe needle (Fig. 1(d)) of 22G (inner diameter of 0.4 mm).

Although the microbead concept has been introduced in [29], this paper presents an extensive characterization of the latest microbead version and includes for the first time: i) its in-vivo proof-of-concept using integrated electrodes (the previous version relied on bulky off-chip cuff electrodes) which is the result of innovative integration techniques, ii) a detailed methodology for the design of better performing transmitter (Tx) and receiver (Rx) coils, iii) a safety limit analysis in a human head model, and iv) a demonstration of individual selectivity to better demonstrate the concept of scattered IMDs in the brain. While multiple microbeads with different capabilities (stimulation and recording), coil diameters (e.g., 300, 200, 180 μm), stimulation-modes (current and voltage-mode), and stimulus waveforms (monophasic and biphasic) were fabricated and tested to satisfy different applications and their requirements, the scope of this paper solely includes the design of a 300 μm stimulating microbead using monophasic voltage-mode stimulation.

The rest of the paper is organized as follows. Section II describes the design details of the microbead. Section III characterizes the Tx and Rx coils. Section IV presents the entire system efficiency. Section V characterizes the integrated electrodes. Section VI presents benchtop measurements. Section VII and VIII provide the proof-of-concept in a conductive medium and in-vivo, respectively. Section IX discusses the comparison between the microbead to the state-of-the-art. Finally, Section X concludes the paper.

II. DESIGN DETAILS

A. System Overview

The system architecture is shown in Fig. 2 and the detailed circuit diagram of the entire system can be found in [29]. The circuit implemented in the microbead is entirely analog. By eliminating the need for data demodulators, decoders, digital control blocks and clock generators, the microbead relinquishes the control of the stimulation pulse amplitude to achieve lower power consumption and further miniaturization [30]. To further reduce the area, the on-chip coil and metal-insulator-metal (MIM) capacitors are placed above the circuit blocks. The ASIC area was also reduced by eliminating the need for a resonating capacitor by making the on-chip inductor resonate with the
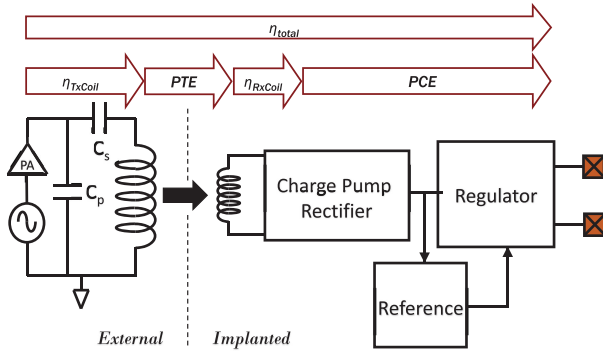
Fig. 2. Drawing of the system architecture of a voltage-mode stimulating microbead. Power efficiencies at different stages of the system are also shown.

coupling capacitors of the charge pump rectifier and the parasitic capacitance of the transistors. The resonant frequency can thus be controlled by changing the width of the transistors in the rectifiers. Common layout techniques to alleviate the effects of process-related gradients have been heavily utilized. This resulted in a maximum resonant frequency variation of 5 MHz, when measuring four identical ASICs.

A pulsed power transmission scheme is adopted, and thus the implant stimulates for every transmitted RF pulse. The amount of charge injected into the tissue (determined by the stimulus pulse width and strength) is linked to the width of the RF pulse. The operating frequency has to be selected carefully as it is one of the most important design parameters for the wireless link. The majority of remotely-powered implants operate in the MHz range to minimize the dielectric loss in tissue. However, resonating at low frequencies requires a large capacitor, which increases the size of the microbead. Therefore, two frequency limits have been set, one being 500 MHz so as to not impact the volume of the implant, and the other 3 GHz in order to keep losses in tissue to a manageable level [31].

The majority of biomedical applications require multiple different stimulating/recording sites to be individually addressable. In this work, this is achieved by assigning a specific resonating capacitance to each microbead making the implants individually addressable, as in a frequency division multiple access (FDMA) system. With 250 MHz spacing between the resonant frequencies, each Tx coil can individually control up to 10 different microbeads within a transmission frequency range of 0.5 GHz to 3 GHz.

B. Design Methodology for the Tx and Rx Coils

This section includes details on the design and optimization of the printed circuit board (PCB) and on-silicon coil. Due to low capture efficiency of the applied fields by the implant's tiny cross-section, maximizing the power transfer efficiency (PTE) is critical and requires the careful design of the Tx and Rx coils.

Although on-silicon coils present their own unique set of challenges, the complexity of the proposed optimization design flow for the 2-coil wireless link remains low, due to the independent (to some extent) optimizing of the external Tx and Rx coil. The design separation is possible because of the ultra-small size of

the receiver and its negligible influence on the Tx coil, which is not the case in most near-field powering systems.

1) Transmitter Coil Design: Two different design procedures are shown in Fig. 3. In step 1, the constraints are considered. It is important to first consider the neural interface application before designing the optimal Tx coil since the brain target region will determine the distance between the Tx and the microbead. The minimum self-resonant frequency (SRF_{Tx_min}) is set to twice the resonant frequency, limiting the Tx coil to a single turn. This eliminates the option of choosing different number of turns, and thus significantly simplifies the optimization flowchart. The surrounding medium has to be determined as well and included in the simulations from the beginning.

Option A is the fastest method in designing the Tx coil as it relies on 3D planar electromagnetic simulators (such as Sonnet from Sonnet Software) which are not as computationally intensive as fully arbitrary solvers. Furthermore, the Tx coil diameter is immediately estimated, and the Rx coil does not need to be included in the simulations (thus allowing for much larger mesh cell sizes). To give a sense of time that it takes to optimize the Tx coil using the proposed design flow, the external coil parameters were found after a simulation of less than 30 minutes using a laptop with a processor speed of 2.5 GHz and 16 GB of RAM. In step 2, the estimated Tx coil diameter is calculated based on the equation from [32]. Note that the Rx coil diameter coil has been removed from the equation, as it is not large enough to impact the result. Additionally, a very large Tx-Rx distance (e.g. applications in human brain) will result in a large Tx coil diameter, which might violate the minimum SRF constraint, in which case the Tx coil diameter is simply set to the highest value possible. In step 3, the quality factor (Q_{Tx}) is maximized by sweeping the width. Step 4 aims to maximize the transmitted power using an impedance matching circuit composed of a series trimmer capacitance (C_s) and a parallel trimmer capacitor (C_p) which allow for the exact tuning to the desired resonance and matches the resistance to that of the power amplifier.

Option B relies on a fully arbitrary 3D electromagnetic simulator (such as ANSYS HFSS) to find optimal design parameters for the Tx coil. Step 2 of the Tx design aims to find D_{Tx_min} which is limited by the size of two capacitors that make up the L-match capacitor network used to maximize the transmitted power and D_{Tx_max} which is limited by SRF_{Tx_min}. In step 3, the coil width and diameter are found by maximizing FOM_{Tx} which is given by:

$$FOM_{Tx} = \frac{|Z_{21}|^2}{Re(Z_{11})} \tag{1}$$

where Z_{11} and Z_{21} are the input impedance and forward transimpedance gain, respectively. Its construction, which can be found in [29], is based on the assumption that the Rx coil diameter is very small compared to that of the Tx. The diameter of the Rx coil is the only parameter which can impact the FOM_{Tx}, thus its trace width and number of turns does not play a role in the Tx coil design. Step 4 is the same as that of Option A.

Going through the design steps (Option B) for a resonant frequency of 1.2 GHz, leads to the following results:
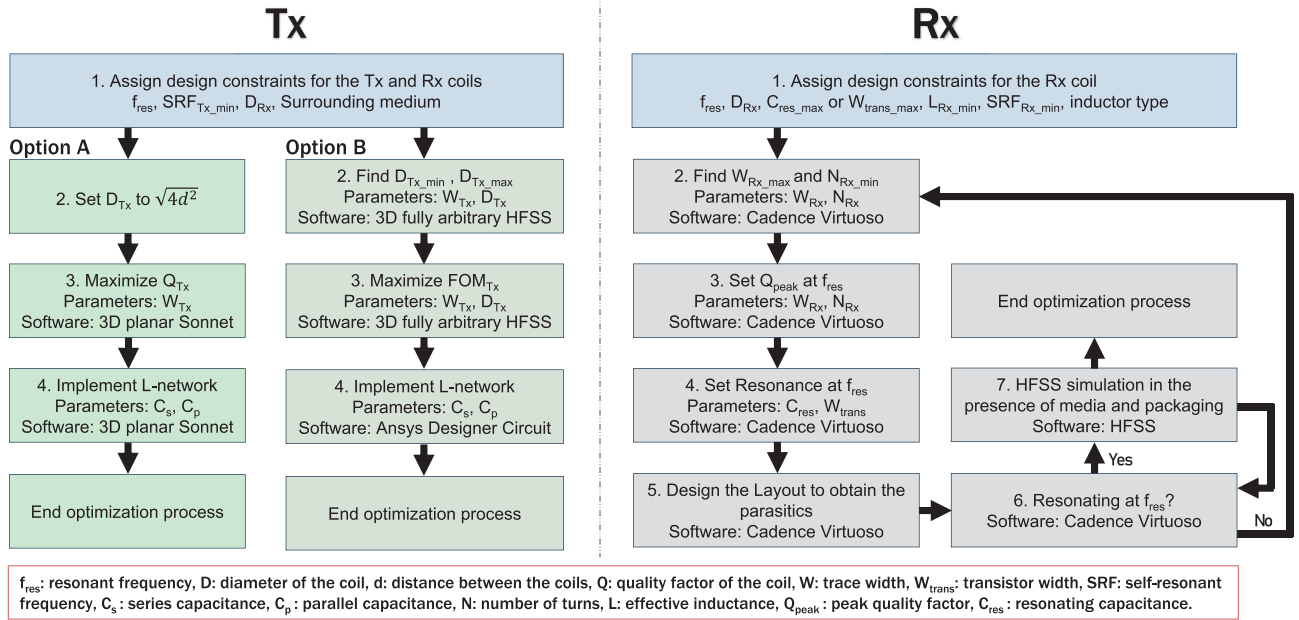
Fig. 3. Two different iterative design optimization flowcharts for the Tx coil (left) and one the Rx on-chip coil (right).

- $D_{Tx\_\min} = 8$ mm and $D_{Tx\_\max} = 15$ mm
- $D_{Tx} = 10$ mm and $W_{Tx} = 3$ mm

Option A design flow provided the same parameter values. It is important to note that this is not always the case as it depends on the design constraint. When the parameters are different Option B provides better performing Tx coils then those with Option A, as it trades off design speed for accuracy.

2) Receiver Coil Design: Only a small percentage of research groups working on wirelessly-powered IMDs have relied on integrated inductors [3], [33], [34]. The main reason is the fact that on-silicon inductors used for energy harvesting have a much lower quality factor (Q_{Rx}) compared to off-chip coils [35] because of the low thickness metallization and losses introduced by the silicon substrate. Despite these drawbacks, the usage of on-chip coils offers significant advantages to floating wireless neural devices because it allows for: i) a smaller implant by eliminating the bulky external Rx coil, ii) good repeatability, iii) a reduction in the number of parts to assemble. Furthermore, the unique sets of challenges (e.g., impact of integrated circuit pad frame on PTE and impact of electromagnetic interference on the PCB traces) of substrate based coils can be addressed as shown in [36].

The design procedure for the on-chip coil is shown in Fig. 3. The aim is to respect the constraints, have a resonating coil and shift the highest quality factor (Q) to the operating resonating frequency. Larger Q comes at the cost of reduced reception bandwidth (BW), which is favorable in this case as it improves the individual selectivity of each resonating microbead.

3D EM solvers such as Ansys HFSS and COMSOL are considered to be the standard tools for the design and optimizing of a wireless coil, but in terms of computation time and accuracy, a better method is to use the parameterized cell (Pcell) provided by the IC foundry. Pcells are modeled based on extensive

measurements results, whereas the accuracy of 3D EM solvers depend on the knowledge of the IC (which can be very limited) and the computation power available. For these reasons, the Rx coil was mainly designed using Cadence. Multiple inductor models are usually offered by the foundry, all of which are very well characterized.

In step 1, the constraints are considered. The Rx coil diameter depends on the device area constraint and is always maximized as much possible. The minimum self-resonant frequency is set to twice the resonant frequency. The maximum transistor width and the maximum resonating capacitance is constrained by the little area left in the ASIC. The values of both parameters determine the minimum coil inductance needed for a targeted resonating frequency. In step 2, the maximum width and minimum number of turns are found in order to set limits on the searching parameters. This is done by sweeping the trace width and number of turns until the values for minimum inductance and minimum SRF are obtained (which were defined in step 1). Increasing the number of turns leads to a larger inductance, but also increases resistance and parasitic capacitance, which leads to a lower SRF. Choosing a larger width for the traces increases Q_{Rx} (because it lowers R_s) but limits the number of turns for a given coil diameter and lowers the SRF by increasing the parasitic capacitance. In step 3, the peak Q is shifted to the resonating frequency. At this point, the geometry of the coil is defined. In step 4, resonance is made possible by sweeping the value of the resonating capacitor. In the special case of the microbead, since the capacitor is eliminated for the purpose of miniaturization, this is achieved by sweeping the transistor's width in the rectifier. In step 5, the layout is designed and the parasitics are extracted. At this stage, there is the option to further increase Q_{Rx} by placing a patterned ground shield underneath it, but this was not done in this work as it would
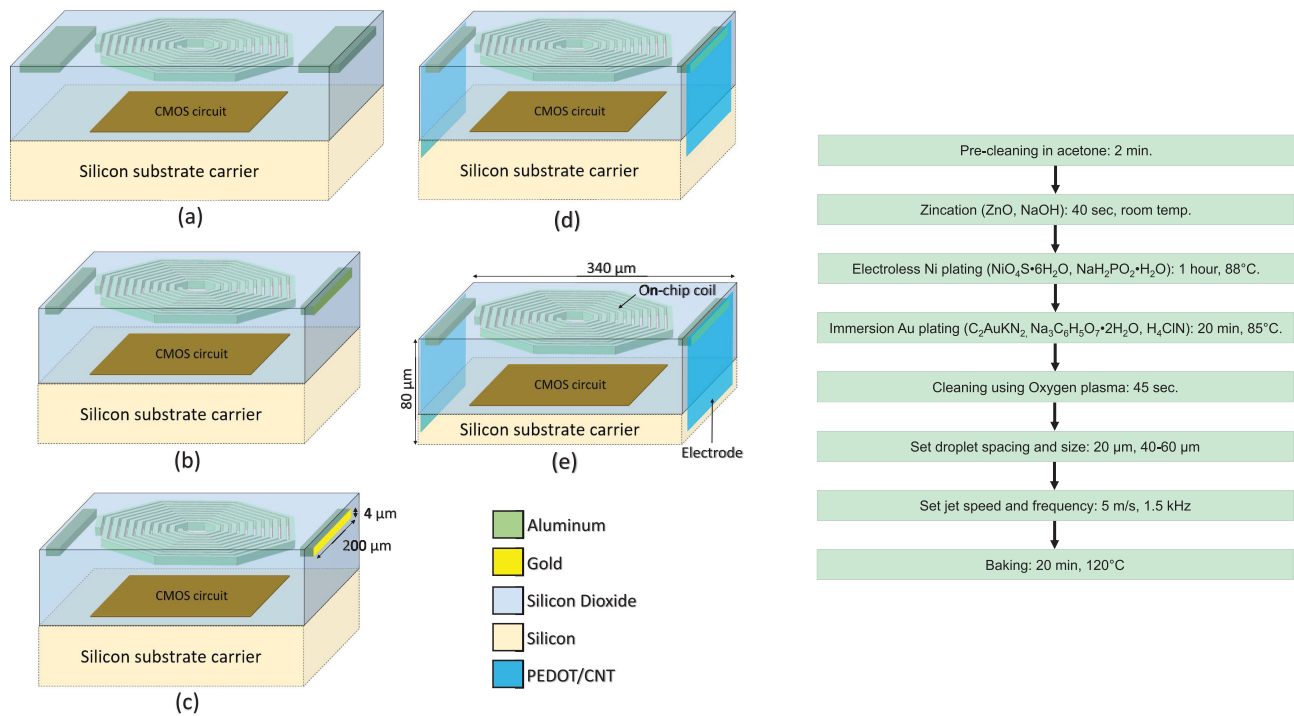
Fig. 4.   Process flow diagram of the microbead electrode integration (left) show the steps after: (a) fabrication by the foundry, (b) dicing, (c) Au immersion, (d) PEDOT:PSS/CNT ink printing, and (e) silicon thinning. Flowchart of the complete Au electroless process and the deposition of PEDOT:PSS/CNT (right).

decrease the SRF of the coil and violate the minimum SRF constraint. In step 6, the Rx coil is simulated with the circuit in order to verify if resonance still occurs at f_{res}. In step 7, HFSS can to be used to account for the presence of media and device packaging, for instance, an IMD has to consider the shift in coil impedance caused by the presence of tissue and the electrode.

C. Electrode Fabrication and Integration

Wirelessly-powered neural interfaces often incorporate multiple different off-chip components such as a coil (or crystal), electrodes and surface mount capacitors. Furthermore, the conventional methods used to connect these components (e.g., flip-chip bonding, wire-bonding and conductive epoxy) to the ASIC increases the volume of the implant and decreases reliability. Therefore, the bulky external parts and the interconnections significantly limit the extent of miniaturization of the packaged implant. One obvious but challenging solution to solving this issue is to fully rely on integrated circuits [37]. A process flow that incorporates all these separate parts into the ASIC chip is shown in the following sections, it was designed such that the microbead does not increase in volume after the electrode integration.

The process flow is described as follows. After receiving the 1.5 mm × 1.5 mm dies from the foundry (Fig. 4(a)), the chips were diced again (while focusing on their edge quality) such that the microbead exposes the top aluminum metal on two sides of the die to act as stimulation electrodes (Fig. 4(b)). The electrode dimensions are 4 μm × 200 μm.

A Zn/Ni/Au stack was deposited on both electrodes (Fig. 4(c)) using an electroless process (Fig. 4) which consists of a series of steps: zincation, nickel deposition, followed immersion gold deposition. Zincation was used to improve the uniformity of the Ni layer and to prevent further oxidation. The sodium hydroxide in the bath removes the native oxide on the Al electrode. The Ni layer provides mechanical backing for the Au layer. During gold immersion, a displacement reaction occurs, in which Ni atoms are replaced by Au atoms. Trisodium citrate and ammonium chloride were added into the bath to act as the complexing agent and stabilizer, respectively. After each step, the die was rinsed in DI water.

Poly-ink HC (purchased from POLY-INK) was then deposited onto the Au electrodes through inkjet printing (Fig. 4(d)). The Poly-ink HC contains an aqueous mixture of conductive polymer and carbon nanotube (CNT), combining the simple processability of PEDOT:PSS with the high conductivity of CNT. The Poly-ink dispersion was passed through a glass fiber syringe filter with a pore size of 0.7 μm and degassed for a few minutes to remove trapped air bubbles before it was loaded into a cartridge. A Dimatix Fujifilm DMP 2800 inkjet printer with 10-pl drop volume cartridges was used. To guide the printing process, images of the microbead were taken on both sides using an optical microscope. Prior to inkjet printing, the silicon-based die was cleaned using oxygen plasma (Technics Micro-RIE Series 800, 150W, 200 torr, 45s). Printing was first done on photo paper to tune the droplet morphology. Multiple cleaning cycles and voltage adjustment were applied until the trajectory of the droplet was stable. The microbead was transferred carefully with a tweezer to a carrier glass slide with the electrode side facing

up. Droplet (drop-to-drop spacing and size) and jet (speed and frequency) settings were chosen based on trial and error. The cartridge and microbead temperature were set to 28 °C. The printed line measures 0.02 mm^2 (other dimensions have been printed as well) and completely covers the Au electrode. After baking the die on a hotplate, it was gradually cooled to room temperature and flipped over with high precision tweezers. The same process was repeated on the other side of the microbead to coat the second electrode.

Once the electrode post-processing was completed, the microbead was thinned down to 80 μm, removing approximately 180 μm of silicon (Fig. 4(e)). This was done using the Multiprep polishing system by Allied. The die was mounted on a small polished metallic stub (prepared in-house), which was mounted on the fixture using thermal wax heated to 150 °C. An adhesive tape instead of the wax could not be used as it would lead to damaging the fragile die during detachment. However, since the silicon surface area that contacts the stub is small, the wax was not able to hold the die in place during grinding. Therefore, in order to increase the contact surface area, the microbead was squeezed between two larger dies. The metallic fixture was then fixated onto the polishing system, and the diamond lapping film placed on the platen. To better anchor the microbead in tissue, the bottom surface of the silicon was made rough by using a large surface roughness (15 μm) for the diamond film. The grinding process was interrupted after 10 sec in order to calculate the silicon removal rate. The total grinding time was 50 sec at a speed of 100 rpm.

Conducting polymers have been often utilized to improve the performance of planar electrodes. In this research, Poly-ink HC has been used to significantly decrease the impedance of the electrodes. However, depositing PEDOT:PSS directly on aluminum will cause unwanted chemical interactions. Therefore, Au was first deposited in order to better interface with the Poly-ink and prevent aluminum from corroding in tissue. It has been shown that PEDOT:PSS/CNT electrodes offer the possibility to stimulate tissue at relatively low voltage and that its adhesion on gold is excellent [38], [39]. PEDOT:PSS deposited using electrodeposition was not possible for the microbead as having to physically contact the microbead in a liquid will significantly increase the complexity of the fabrication process flow. It was for that reason that the polymer is deposited using ink jet printing, an unconventional technique but an effective one in this situation.

Having the electrodes on the sidewalls of the CMOS die maximizes the anode-cathode separation and thus the stimulation effect. Similarly, in the case of a recording microbead, the recording and reference electrode separation is also maximized, which increases the signal to noise ratio of the recording signal. As for the area of the electrode, although the width of the surface CMOS electrode is not a controllable parameter, its area is significantly increased by the added conductive ink. The maximum electrode area is determined by the thickness of the microbead and thus the silicon removal step. A larger electrode surface area will increase the current peak of the stimulation pulses but will reduce to maximum stimulation rate (as it takes longer to charge and discharge the electrode capacitance). The neural interfacing application also determines the electrode

TABLE I
CHARACTERIZATION OF THE TX AND RX COIL

Parameter	Tx	Rx
Diameter (mm)	10	0.3
Material	*Cu*	*Al*
Trace width (mm)	3	7e-3
Trace thickness (μm)	35.6	4
Space between turns (mm)	*N/A*	5e-3
Number of turns	1	7
f_{res} (GHz)	1.18	1.18
Q at f_{res} in air	359	12.2
L at f_{res} in air (nH)	8	25
SRF (GHz)	4.1	2.5

area, for instance, applications focusing on selectivity and spatial resolution would require a smaller stimulating electrode area in order to recruit fewer neurons. For these reasons, different electrode sizes were fabricated in this work.

III. COIL CHARACTERIZATION

A. Measurement Setup

Characterization of the Tx and Rx coil was done using a vector network analyzer (ZVL, Rohde & Schwarz). In addition to the VNA, the measurement setup for the on-chip coil also required a micromanipulator probe station and an RF probe (Z10-GS-150; Cascade Microtech). For accurate measurements, the parasitic effect caused by the coaxial cable, probe, pads, and the feed lines were removed during the de-embedding calibration procedure (on-chip short/open/50Ω). Same goes for the Tx coil, the parasitics from the SMD connector and cable were eliminated.

B. Measurement Results

Measured characteristics of the Tx coil and Rx coil are summarized in Table I.

The transmitter coil was built on FR4 substrate. The PCB also contains the L-match capacitor network to maximize the transmitted power and an SMP connector. Rather than soldering the connector and the capacitors on PCB traces leading to the coil, they were directly placed on top and below the coil, which shortened the inductor but allowed more of the source energy to be picked up by the microbead. Eliminating the interconnects also allowed the Tx coil to become more symmetrical such that it can be used in a coil array for near-field beamforming [40].

Fig. 5 compares the measured fitted quality factor and effective inductance of a 300 μm diameter coil with simulations done in Cadence tool. Measurement results are in good agreement with Cadence simulations. The small mismatch is mainly caused by the de-embedding imperfections at high frequencies. The dual layer series stacked inductor Pcell has been chosen for this work as it allows the effective inductance to be high while avoiding placing the capacitors directly underneath the inductor, which degrades the Q. Thus, when including the entire circuitry of the microbead, the quality factor drops by only 1.2 compared to a stand-alone coil. The inductance and quality factor drop more
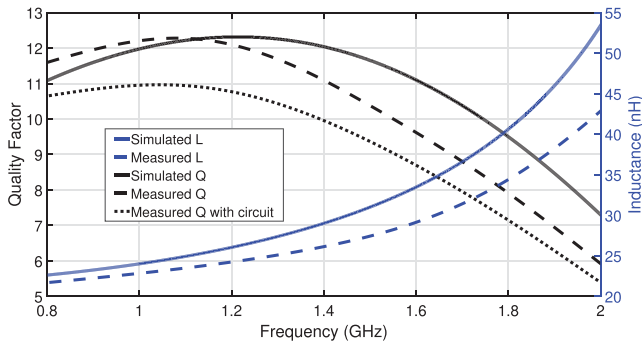
Fig. 5. Measured and simulated quality factor and effective inductance of the 300 μm on-silicon coil.

Microbead #	1	2
Rx resonant frequency (GHz)	1.25	1.5
Tx-Rx Distance (mm)	4.6	
Medium	Tissue (beef)	
Lateral Misalignment Δx (mm)	+2	-2
Voltage (V) when f = 1.25 GHz	1	0.31
Voltage (V) when f = 1.5 GHz	0.15	1

significantly when directly placing the MIM caps underneath the coil as shown in [29].

IV. SYSTEM EFFICIENCY AND IMPLANT SELECTIVITY

A. Measurement Setup

It is very challenging to measure the PTE involving an ultra-small Rx coil as any connection to the on-chip coil will add parasitics and behave like a bigger inductive loop. This is due to the fact that the size of the Rx coil is in the deep sub-mm scale, whereas the bondwires and PCB traces are in the mm to cm range. Therefore, rather than finding the RF-RF efficiency (also known as PTE in this work), the RF-DC efficiency is measured as the parastics added by the pads, bondwires and PCB traces do not affect the measured DC voltage.

In this work, the full system efficiency (η_{total}) is defined as the ratio of power delivered to the resistive load to the transmitted source power set by the power generator. The overall efficiency thus includes several loss factors, which are the power loss: *i)* in the Tx coil (η_{TxCoil}), which also includes that of the PA and coaxial cable, *ii)* between the Tx and Rx coil (PTE), *iii)* in the Rx coil (η_{RxCoil}), which also includes power reflected by resistance mismatch, and *iv)* in the harvesting circuitry (PCE), which comprises a charge pump rectifier, a reference voltage, and a regulator. The product of all efficiencies (Fig. 2) are given by: $\eta_{\text{total}} = \eta_{\text{TxCoil}} * PTE * \eta_{RxCoil} * PCE$. Efficiency measurements were obtained by sweeping the source power at 1.18 GHz until the Rx device reached its regulated voltage of 1 V.

To mimic the lossy tissue media in one of the setups, the microbead was entirely engulfed in beef by placing the tissue above and underneath the PCB. The CMOS chip was partially encapsulated in epoxy (EPO-TEK 353ND-T) such that the bond-wires are protected from the tissue while leaving the microbead exposed. The purpose of this was to create a physical contact between the wet tissue and the microbead, as would occur in a real scenario.

As mentioned earlier, an FDMA approach is implemented to individually address the microbeads. Two microbeads resonating at different frequencies (1.25 and 1.5 GHz) were individually selected to demonstrate the idea. They were wirebonded onto a PCB and wirelessly powered through tissue. The center of the

Tx coil was placed in the middle of two dies in order to create a lateral misalignment of 2 mm for each of the Rx coils. This was done to simultaneously measuring the voltage generated by both microbeads while the power transmitting frequency toggled between the two resonant frequencies.

B. Measurement Results

Fig. 6 shows the measured overall efficiency as the microbead was moved away from the Tx coil. The amount of power delivered to the load (PDL) was changed four times to demonstrate the PCE dependence on the stimulus amplitude. As stimulation is an energy-intensive function (much greater than neural recording), large PDL values were chosen. This particular charge pump rectifier performs better as the source power increases.

Fig. 6 also shows the measured overall efficiency when 5 mm of tissue was placed between the Tx coil and microbead, and 2 cm of tissue placed underneath the PCB. This experiment was done for two reasons: emulate to some extent the performance of a microbead in the cortex and quantify the difference between air and tissue medium. Although some of the transmitted power is lost in tissue, the setup with tissue shows larger efficiencies. This unusual response is explained by the fact that the medium is considered during the design of the microbead. In tissue, the microbead's resonant frequency is closer to 1.18 GHz than when placed in air. Furthermore, the resistance of the coil is better aligned with that of the rectifier when tissue is present, leading to less signal reflection caused by mismatched impedances.

As shown in Table II, the difference between the generated voltages are 700 mV when microbead#1 is selected and 850 mV when microbead#2 is selected. The cross-talk is small enough as long as the transmitted power is kept to a minimum (Psource$_{\text{min}}$). In other words, for the FDMA approach to work effectively, the transmitted power needs to be adjusted until the addressed microbead receives the minimum amount of power to generate the necessary current. To locate Psource$_{\text{min}}$, a closed-loop system is needed, in which the feedback (e.g., neural recording, backscattering, subject's behavior, etc.) notifies when the microbead has turned "ON". As for applications that require microbeads inserted at different depths under the same Tx coil, the cross-talk can be reduced by having microbeads that are inserted at shallow depths use the lower frequency band and microbeads that are implanted deeper use the higher frequency band.
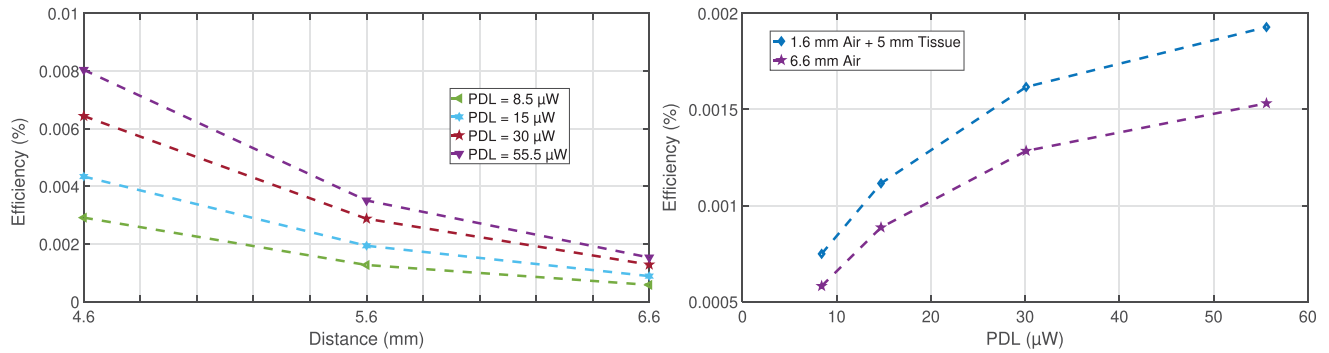
Fig. 6.   Measured efficiency at 1.18 GHz as a function of Tx-Rx distance for different PDL values (left). Measured efficiency in air and tissue as a function of PDL for a Tx-Rx distance of 6.6 mm (right).

V. Electrode Characterization

A. Measurement Setup

The electrochemical impedance spectroscopy (EIS) was used to measure the impedance of the novel electrodes using a VSP-300 potentiostat (Bio-Logic Science Instruments) with a two-electrode system. Poly-ink served as the working electrode and a large Pt electrode as the counter electrode. A PDMS (1:10) chamber was glued onto printed Poly-ink lines (with different surface areas) by using low toxicity silicone adhesive (World Precision Instruments) and filled with 1x phosphate-buffered saline (PBS). Outside the chamber, a thin copper wire was connected to the Poly-ink line with eutectic gallium indium (EGaIn). The EIS measurements were made over a $1–10^5$ Hz frequency range using a 10 mV sinusoidal excitation voltage. The impedance spectrum is presented as a Bode plot using log spacing for |Z| and frequency Fig. 8.

B. Measurement Results

Micrographs of the microbead's surface which contains one of the two electrodes are shown in Fig. 7 at different stages of post-processing. Microbeads of different thicknesses (63, 80, 114, 130, and 146 μm) were successfully fabricated, Fig. 7(d) shows the thinnest of them all. As the ratio of the implant's length to the implant's thickness increases, the ASIC chip becomes more fragile and thus harder to handle. The final dimensions of the microbead that has been experimentally demonstrated in this paper are 340 μm $\times$ 330 μm $\times$ 80 μm, giving it a volume of approximately 0.009 mm^3 (Fig. 7).

Fig. 8 illustrates the EIS plot for 3 electrode surface areas: 0.05 mm^2, 0.025 mm^2, 0.02 mm^2, with impedance (at 1 kHz) of 3.8 kΩ, 5.9 kΩ, and 8.2 kΩ, respectively. At low frequencies, the Poly-ink exhibits a predominantly capacitive phase angle ($-80°$), thus the electrode typically behaves like a capacitor. Capacitor electrodes provide a safer stimulation mechanism as they rely on charge redistribution rather than charge transfer. The equivalent circuit model of the electrode-electrolyte interface of the 0.02 mm^2 electrode is shown in Fig. 8, in which R_s is the spreading resistance, C_{dl} is the double layer capacitance. Both parameters heavily depend on the surface area of the electrode.
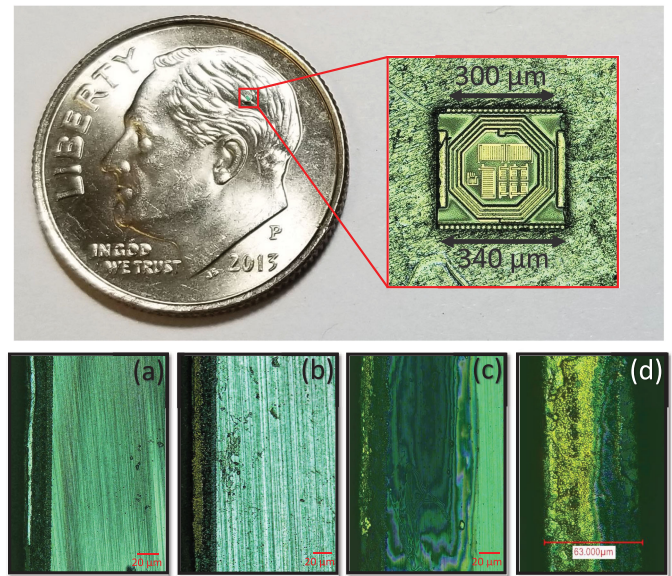

Fig. 7.   Top-view micrograph of the microbead with the integrated electrodes (top). A U.S. dime is shown as a scale reference. Side-view micrographs of the microbead at different stages of post-processing (bottom) after: (a) dicing, (b) Au immersion, (c) Poly-ink printing, and (d) backside thinning.

Due to the non-ideal capacitance response, C_{dl} can be replaced by a constant phase element, however, for simplicity C_{dl} is kept as it provides a satisfactory fitting curve as shown in Fig. 8. By using low-impedance electrodes, the microbead can operate with a V_{DD} of 1 V. A much larger regulated voltage would have been problematic since the charge pump rectifier would have needed more stages resulting in a decrease in PCE, and thus increase in power transmitted.

VI. Monophasic Stimulation Benchtop Measurement

A. Measurement Setup

The Poly-ink electrode equivalent circuit model has been implemented using discrete passive components (250 nF, 8 kΩ, 8 kΩ, 250 nF) to measure the stimulation current of the microbead while being wirelessly powered. The generated current
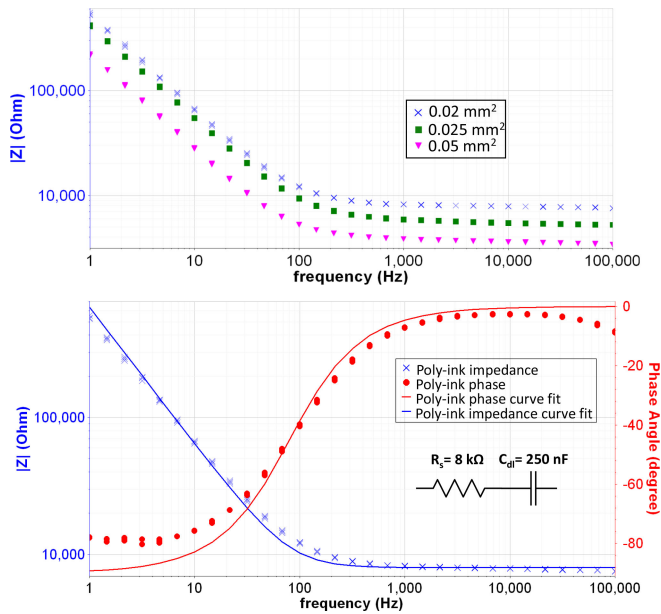
Fig. 8. Impedance measurement bode plots of: Poly-ink electrodes of 3 different dimensions (top) and a 0.02 mm^2 Poly-ink electrode with the equivalent circuit model of the electrode-electrolyte interface (bottom).
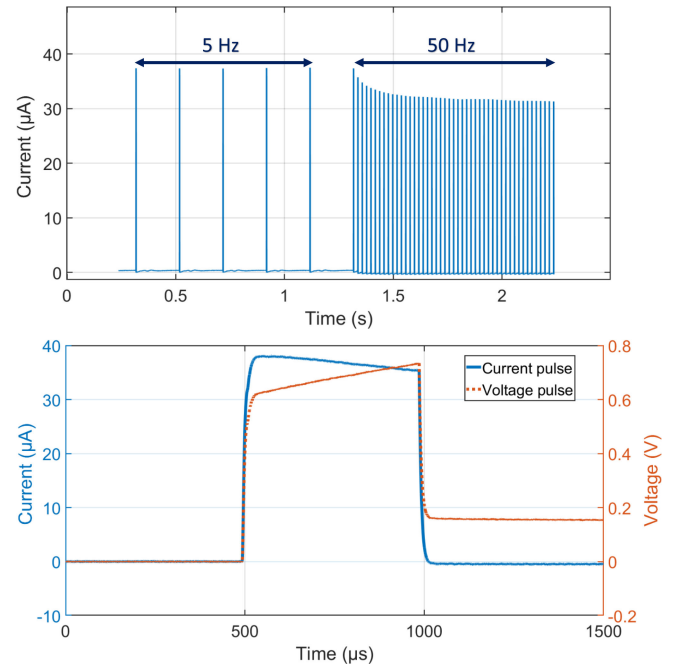

Fig. 9. Measured monophasic current pulse(s) of the microbead in voltage-mode stimulation, while being powered wirelessly and connected to the electrode-electrolyte equivalent circuit model: current pulses at 2 different frequencies (top), and zoomed-in view of a single current and regulated voltage pulse (bottom).

pulses provide a good idea of what to expect when the microbead is implanted in tissue. The Tx coil was placed 6.6 mm above the microbead and the power amplifier supplied 36 dBm of power to the Tx coil at 1.18 GHz. The RF power pulse had a frequency of 5 Hz and a pulse width of 500 us. After transmitting four pulses, the frequency was changed to 50 Hz.

B. Measurement Results

Fig. 9 shows a single current pulse with a width of 500 μs and a peak current amplitude of 38 μA, leading to a calculated injected charge of 18 nC (0.09 mC/cm^2), which is more than what is typically needed to activate neurons in the CNS and is well below the charge injection capacity reported for PEDOT:PSS [41]. The injected charge can be significantly increased (i.e, $>$ 60 nC) if more is needed as the required charge to elicit an action potential is not a fixed quantity since it depends on multiple parameters such as the distance between the electrode and the target neural structure, the shape of the stimulus pulse and the properties of the neural tissue. The ability to increase injected charge by controlling the pulse width is also critical because of the larger driving voltages required to deliver stimulation pulses in-vivo. It is important to note that with larger pulse widths or larger transmitted power, the voltage pulse reaches its maximum amplitude of 1 V. Limiting the maximum voltage across the Poly-ink electrode sets a limit on the maximum polarization potential, and thus prevents water from hydrolyzing, which causes damage to the electrodes and surrounding tissue.

Due to the dominant capacitive component of the electrode-electrolyte interface, the current has an exponentially decaying waveform (which can be better observed for larger pulse widths). After the microbead was turned OFF, at the end of the monophasic stimulation pulse, the electrode discharges over a time course

determined by the tissue resistance and electrode capacitance. As can be noticed from the figure, the voltage at the electrode (which is the regulated voltage) decreases very slowly, fortunately, this does not prevent the microbead from reaching stimulation rates over 200 Hz, covering the high frequency bands used for clinical applications such as the treatment obsessive compulsive disorder, depression, and Parkinson's disease. However, this comes at the price of smaller current peaks ($<$30 μA), since the voltage across the electrodes is diminished.

VII. PROOF-OF-CONCEPT DEMONSTRATION IN CONDUCTIVE MEDIUM

A. Measurement Setup

The purpose of validating the free-floating microbead in a conductive aqueous environment is to show: *i)* that it can still be turned ON while currents are leaking into the substrate (as the implant is not hermetically sealed with an added coating), *ii)* the ability of native silicon dioxide to act as a barrier against the permeation of water vapor for a short period of time, and *iii)* the formation of a voltage gradient across its Poly-ink integrating electrodes.

Fig. 10 shows the setup used for the validation in PBS. The chamber surrounds a MEA that measures 800 μm $\times$ 800 μm. The MEA consists of 60 electrodes, each composed of multiple PEDOT:PSS pillars [42]. The measured impedance of each electrode at 1 kHz is around 200 kΩ. The microbead is dropped inside the chamber containing 1x PBS. Since the silicon chip is floating on the surface of the PBS, the microbead is not aligned
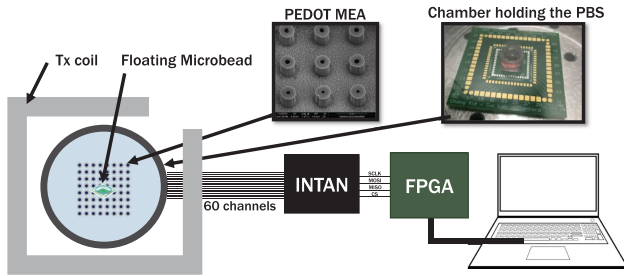
Fig. 10. Top view of the measurement setup used to indirectly record the voltage generated by the wirelessly powered microbead floating in PBS.
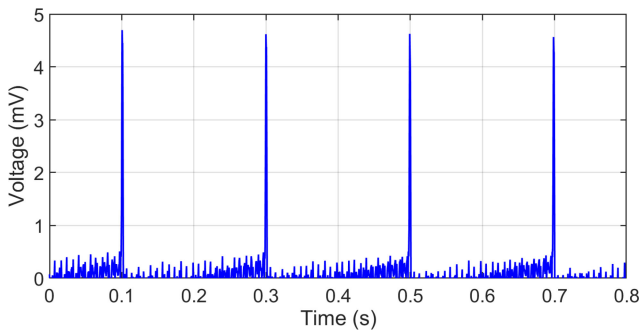

Fig. 11. Voltage recordings of the Intan chip when the microbead was floating in PBS while being wirelessly powered.

with the Tx coil and its location is unpredictable. Therefore, a MEA was used instead of a single electrode pair in order to guarantee that at least one PEDOT:PSS electrode is located directly underneath the free-floating device. Two Intan chips (RHD2164, Intan Technologies Inc., USA) were used to amplify and digitize the acquired signal coming from 60 recording channels. The commercially available chip was chosen as it offers programmable sampling rate and filtering along with high input impedance, accurate gain, and good common-mode signal rejection. An XEM 6010 Opal Kelly board then receives the processed signal and transfers it to a computer. The whole setup is battery powered in order to minimize the 60 Hz noise. The Tx coil was placed 6.6 mm above the PBS surface (and thus the microbead) and the power amplifier supplied 36 dBm of power to the Tx coil at 1.18 GHz. The RF power pulse had a frequency of 5 Hz.

B. Measurement Results

Fig. 11 shows the voltage recorded by the Intan chip using a PEDOT:PSS electrode. Although it is not a direct measurement of the voltage generated by the microbead, it does hint that the microbead has reached its regulated voltage of 1 V. This was deduced by replacing the microbead with a pair of electrodes connected to a 1 V voltage source, which resulted in a recording of 5 mV. It can also be concluded that moisture will not damage the implant during acute experiments as the exact same plot was obtained after leaving the microbead in PBS for approximately 6 hours.

VIII. PROOF-OF-CONCEPT IN-VIVO EXPERIMENT

A. Measurement Setup

To test the microbead in practical use with the integrated electrodes in a biological environment, an animal experiment has been conducted. Although the microbead is designed for the stimulation of the central nervous system (CNS), having the microbead fully implanted in the sciatic nerve of a rat confirms its ability to elicit action potentials in axons. The surgical procedures used for electrical stimulation and monitoring of peripheral nerves in rats were approved by the Johns Hopkins Medical Institute Animal Care and Use Committee (ACUC). A Male Wistar rat was given an intraperitoneal injection of ketamine/xylazine cocktail (0.1 mL/100g). After dissecting and exposing the left sciatic nerve, a piece of rubber from a surgical latex glove was gently placed under the nerve. The electromyographic (EMG) activity evoked in the gastrocnemius muscle of the lower leg was recorded using hook intramuscular electrodes (Motion Lab Systems, CA, USA). The signals were amplified and digitized with a preamplifier (RA16PA, Tucker-Davis Technologies, Alachua, FL). A pocket was created on the side of the nerve, large enough for the microbead to slide in. After positioning the Tx coil on top of the rat's leg, the capacitors are tuned for impedance matching and resonance. A formable coaxial cable was used so that the Tx coil remains impedance matched to the amplifier during the duration of the experiment. The Tx-Rx distance is estimated to be around 5 mm. The system was turned "ON" and "OFF" at frequencies of 1 Hz and 5 Hz. An RF signal generator (SMBV100A, Rohde & Schwarz) connected to the power amplifier supplied 36 dBm of power to the Tx coil at 1.18 GHz. In order to control the duty cycle using pulse modulation, a 100 MHz arbitrary function generator (AFG3102, Tektronix) was connected to the RF generator. Monophasic current pulses with a width of 500 μs were delivered using the integrated 250 μm $\times$ 80 μm (0.02 mm^2) electrodes.

Fig. 12(a) shows a drawing of the experimental setup in order to clearly illustrate the different instruments and components used during the in-vivo testing. The fully implanted microbead is shown in Fig. 12(c). In order to better visualize the implant, it is shown again in Fig. 12(d), after placing it at very close proximity to the surface of the nerve.

B. Measurement Results

The EMG response to voltage-mode bipolar stimulation is shown in Fig. 13. Each voltage spike represents a muscle response; the width of the EMG response is about 20 ms, which explains why they appear as spikes in the 6 sec plot. It takes about 5 ms for the response to appear after the microbead is wirelessly turned ON. As the distance between the integrated electrodes is only 340 μm, the fully implanted microbead allows precision targeting of nerve fibers. The localized stimulation also explains why the artifact is barely visible in the EMG plot. On the other hand, when a cuff electrode that envelops the entire nerve is used, it has been shown [29] that sufficient current is induced wirelessly to cause the entire hindlimb to move.
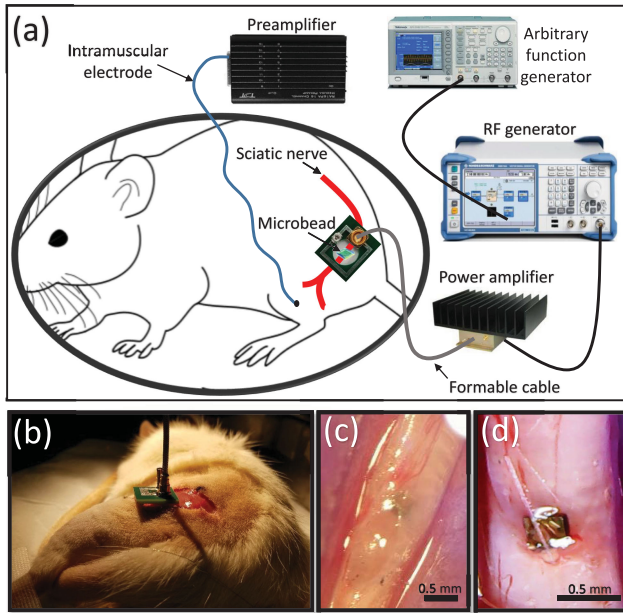
Fig. 12.   (a) Drawing of the experimental setup for in-vivo testing. Picture of (b) the anesthetized rat and the Tx coil, (b) the microbead implanted half way through the sciatic nerve, and (d) when implanted at shallow depths.
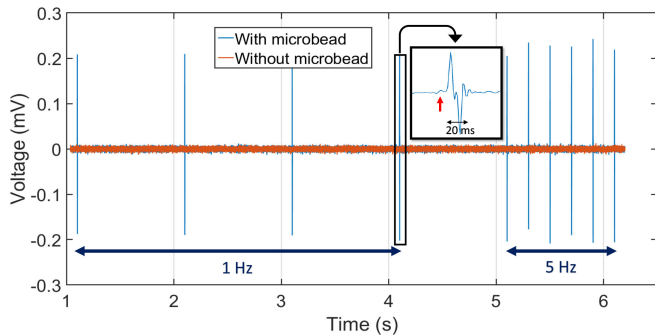

Fig. 13.   EMG response to voltage-mode bipolar stimulation at 1 Hz and 5 Hz repetition rate and a close-up view of a single EMG response with stimulus artifact indicated by an arrow.

It is important to note that while the Tx coil was positioned such that the external coil center was aligned with the Rx coil center for maximal efficiency, this was difficult to verify, and a lateral displacement of up to 2 mm is possible, which can result in a large attenuation in received power as shown in [36]. A rotational misalignment of at least 20 degrees is also expected.

IX. DISCUSSION

A. Wireless Powering Performance Comparison to the State-of-the-Art

Table III compares the wireless powering efficiency of the microbead with that of state-of-the-art ultra-small receivers (≤ 0.5 mm^2). A straightforward comparison is difficult as the Rx coil area, Tx-Rx distance and medium are all different from one another. In order to make a fair comparison with other published

results, a FOM (equation 23) has been proposed in [33]:

$$FOM = \frac{\eta \times d^3}{A^{1.5}} \qquad (2)$$

where, d is the Tx-Rx distance, and A is the Rx coil area.

It is important to note that although this FOM is widely used in the field when Rx coil dimensions are much smaller than the Tx coil, it does not take into consideration the operating frequency, the wireless system, the PDL, and the medium. Nevertheless, among the 2-coil wireless systems in the field, the microbead has one of the highest FOM's considering the operating frequency it is using.

Since the relative permittivity of brain tissue is much higher compared that of air, the wavelength at the operating frequency of the microbead is significantly reduced once it reaches tissue. For instance, for a transmitted power frequency of 2 GHz, the wavelength is 15 cm in air and around 2 cm in the grey matter. Depending on the implantation depth (d) and the frequency of the power signal, the microbead can either be in the reactive near-field ($d < \frac{\lambda}{2\pi}$), the radiating near-field ($\frac{\lambda}{2\pi} < d < \lambda$), or the mid-field ($d \approx \lambda$). The field variation impacts the PTE, but does not influence the described Tx and Rx coil design methodology. With better designs in the future, the achievable depth will increase, but in this work the measurements in air and tissue are done using small Tx-Rx distances (<1 cm), thus keeping the microbead in the near-field region.

B. Performance Summary and Comparison to the State-of-the-Art

Numerous wirelessly powered single-channel neural stimulating implants have been fabricated [19]–[26]. Table IV summaries and compares the microbead performance with the smallest (<50 mm^3) among them. The microbead is 50 times smaller than the second smallest neural stimulating implant reported in the comparison Table. The microbead extreme miniaturization puts a heavy limit on its implantation depth. Yet, owing to its optimized wireless inductive link, the FOM (Depth/Volume) remains large compared to the state-of-the-art. However, the FOM only provides a rough idea on the performance of the different types of implants as it can be further increased by increasing the transmitted power (and thus depth) until the SAR limit is reached. Therefore, it should not be solely relied upon for comparison.

It is also important to note that the smallest miniaturized stimulators have so far been validated only in sciatic nerves. For some of these devises, implanting them into the brain will result in a much smaller achievable in-vivo depth. IMDs powered by acoustic waves are the ones to see the biggest attenuation in wireless link efficiency due to the fact that the bone has very high attenuation coefficient to ultrasonic beams.

The microbead is small enough to enable direct injection into the target brain region via a syringe needle. During a stereotactic surgery, this method allows for precise and minimally-invasive insertion into the cortex and subcortex. In the next iteration of this work, a custom-made needle will be fabricated to ensure that the IMD is inserted at the correct orientation. Another viable

TABLE III
WIRELESS POWERING PERFORMANCE SPECIFICATIONS OF THE MICROBEAD IN COMPARISON TO OTHER STATE-OF-THE-ART
ULTRA-SMALL RECEIVERS (≤ 0.5 mm^2)

Ref.	Rx coil area (mm^2)	Rx coil type	Tx-Rx distance (mm)	Wireless system	Medium	Frequency (GHz)	FOM (2)	η_{total} (%)
[43]	0.5	On-chip	0.5	2-coil	Air	2.5	0.013	0.038 PDL = 94.7 μW
[44]	0.25	On-chip	8	3-coil	Liquid phantom	0.915	77	0.019 PDL = 95 μW
[34]	0.125	On-chip	1	2-coil	Air	1.5	0.48	0.021 PDL = 10.5 μW
[45]	0.01	On-chip	1.2	2-coil	Air	2	2.76	0.0016 PDL = 100 μW
This work	**0.09**	**On-chip**	**6.6**	**2-coil**	**Tissue (beef)**	**1.18**	**20.4**	**0.0019* PDL = 55.5 μW**

*in addition to the rectifier, the PCE also includes the efficiency of the charge pump, voltage reference, and voltage regulator.

TABLE IV
PERFORMANCE SUMMARY COMPARISON WITH STATE-OF-THE-ART ULTRA-SMALL (<50 mm^3) WIRELESSLY POWERED NEURAL STIMULATING IMPLANTS

Reference	[23]	[24]	[25]	[26]	**This work**
CMOS process (nm)	180HV	65	-	N/A	**130RF**
Stimulation mode	current	current	switched-cap.	voltage	**voltage**
Wireless link	ultrasound	ultrasound	2 coil inductive	2 coil inductive	**2 coil inductive**
Frequency (MHz)	1.3	1.85	394	10	**1180**
Charge balance	biphasic	passive recharge	biphasic	none	**none**
Compliance voltage (V)	15	3	N/A	N/A	**N/A**
Electrode material	Pt	PEDOT	PtIr	Pt	**PEDOT:PSS/CNT**
Surface area (mm^2)	3.3	0.3	0.79	0.07	**0.02**
Impedance (kΩ) at 1 kHz	< 1	4*	-	-	**8.2**
Max. current density (A/cm^2)	0.15	0.13	-	0.57	0.23
Animal model	(ex vivo) frog sciatic	rat sciatic	rat peroneal	rat sciatic	**rat sciatic**
Fully-implanted	no	yes	yes	yes	**yes**
In-vivo depth (mm)	-	20	-	50	**5**
Off-chip components	capacitor, piezo, LED, and electrodes	capacitor, piezo, and electrodes	diodes, ind. and electrodes	no ASIC used	**none**
Implant encapsulation	PDMS	parylene	SU-8	epoxy	**SiO$_2$**
Mass (mg)	78	10	-	-	**< 1**
Volume (mm^3)	39**	2.2	1.39	0.45	**0.009**
FOM$_{Depth/Volume}$ (mm^{-2})	-	9.1	-	111	**555**

**does not include the electrodes
*provided for 2.5 kHz

option would be to attach the IMD to the tip of a pillar using biodissolvable adhesive.

The described process flow, which allows the integration of the electrodes without having to increase the volume of the ASIC is simple and relatively inexpensive to implement as it does not require a micro-fabrication facility. It is important to note that the fabricated prototype is intended for acute experiments and will need a hermetic biocompatible coating to survive the harsh tissue environment. However, this step is not a priority in the initial stages of this work as there are more important challenges to address first. The fabricated microbead relies on the native oxide (on the remaining silicon bulk) to prevent short circuits from occurring in tissue, however, the oxide is not thick enough (<3 nm) to prevent small current paths between the electrode and grounded substrate. The leaked current is estimated to be only a few microamps, which is large enough to make a noticeable impact on the overall system efficiency. This issue can be solved by porting the device to a silicon-on-insulator (SOI) process as described in detail in [29].

C. Safety Limit Analysis

Although an experimental proof-of-principle has been presented in a rat model, one of the long-term applications of this work is to have the microbead implanted in human subjects as they would benefit the most from an untethered device. Therefore, it is important to know if the transmitted power level respects the limit for safe exposure to radio-frequency
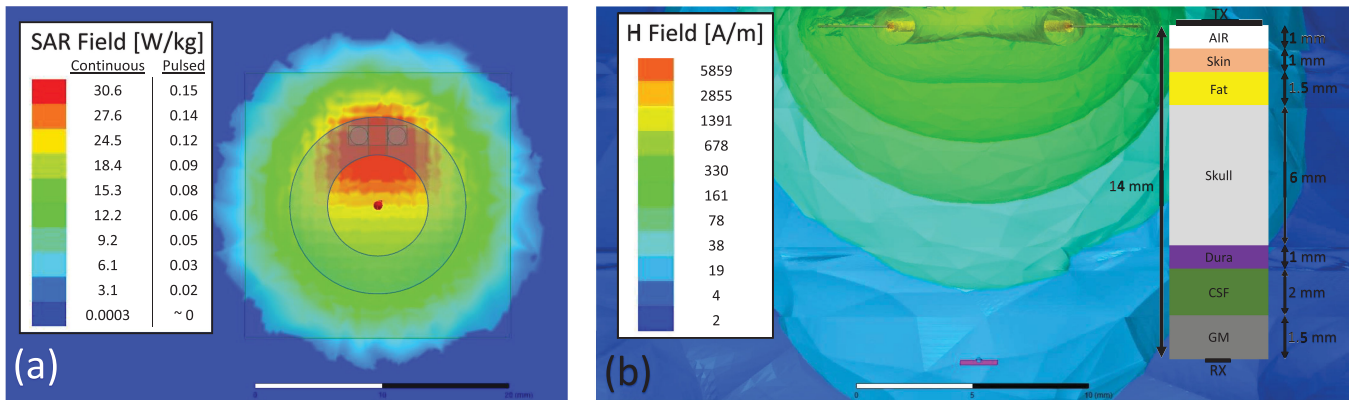
Fig. 14.   Top-view and side-view of the HFSS (a) SAR and (b) H-field simulations at 1 GHz. The model includes the transmitter coil, receiver coil and the 6-layer head model.

energy. To prevent tissue heating, the Federal Communications Commission (FCC) in the United States has set the specific absorption rate (SAR) limit to 1.6 W/kg, which is an average over a time period of 6 minutes for the head over any 1 g of tissue. SAR is given by the following equation:

$$SAR = \frac{\sigma \, |E|^2}{\rho}$$

where σ and ρ represent conductivity and mass density of the exposed tissue. E is the electric field strength in the tissue.

The local SAR values were simulated using HFSS built-in SAR function using a 6-layer head model (skin, fat, skull, dura, cerebrospinal fluid, and grey matter) as shown in Fig. 14. The Tx coil has a diameter of 14 mm, a trace width of 3 mm and a trace thickness of 0.25 mm. The Tx-Rx coil distance was set to 14 mm, which is the average depth it takes to implant the microbead into an adult human cortex. The on-chip coil has a gain of -55.72 dB at 1 GHz. Therefore, the transmitted source power is set to 46 dBm in order to capture -10 dBm of power at the microbead.

When continuously transmitting 46 dBm of power 1 mm above the human head, HFSS simulations show a maximum SAR value of 30.6 W/kg at the skin level. Fortunately, for neurostimulation applications, the duty cycle does not exceed 2% of the stimulation period. Since a pulsed powering scheme is implemented (like during magnetic resonance imaging scans), power is only transmitted for a very short amount of time, allowing the different layers to cool down during the off period. For instance, when stimulating at a repetition rate of 10 Hz with a current pulse width of 500 μs, the maximum average SAR over 6 minutes becomes 0.15 W/kg. The large headroom available before the SAR limit is reached provides the freedom to increase the implantation depth and the stimulation rate. The headroom is also needed for unavoidable misalignment that will occur once the microbead is implanted.

X. CONCLUSION

A new generation of neural interface is needed to open up a wide range of potential applications that are currently not possible. In this work, the development of an ultra-small ($\sim$0.009 mm³) neural implant device and its experimental proof-of-concept has been reported. To allow for minimally-invasive insertion into the cortex and subcortex, the microbead has been extensively miniaturized by minimizing the area of the system using simplification and aggressive layout design techniques, and by implementing a novel packaging method to allow the microbead to become a fully encapsulated stand-alone implant. In order to increase the implantation depth of the SoC, the power consumption has been minimized by improving the PCE and the inductive link has been strengthened owing to a new optimization design flow of the Tx and Rx coils. The microbead has the potential to replace conventional techniques for brain stimulations, particularly in studies involving many neurons from many areas distributed around the nervous system. The presented work is to be seen as the initial steps taken in achieving the goal of safely powering ultra-small implants. Although there are still numerous obstacles to overcome, the future of fully injectable single channel neural interfaces looks promising.

REFERENCES

[1] A. M. Sodagar, G. E. Perlin, Y. Yao, K. Najafi, and K. D. Wise, "An implantable 64-channel wireless microsystem for single-unit neural recording," *IEEE J. Solid-State Circuits*, vol. 44, no. 9, pp. 2591–2604, Sep. 2009.

[2] X. Xie *et al.*, "Long-term reliability of al2o3 and parylene c bilayer encapsulated utah electrode array based neural interfaces for chronic implantation," *J. Neural Eng.*, vol. 11, no. 2, 2014, Art. no. 026016.

[3] S. Ha *et al.*, "A 16-channel wireless neural interfacing SoC with RF-powered energy-replenishing adiabatic stimulation," in *Proc. VLSI Circuits Symp.*, 2015, pp. C106–C107.

[4] P. Troyk *et al.*, "In-vivo tests of a 16-channel implantable wireless neural stimulator," in *Proc. IEEE 7th Int. IEEE/EMBS Conf. Neural Eng.*, 2015, pp. 474–477.

[5] L. Karumbaiah *et al.*, "Relationship between intracortical electrode design and chronic recording function," *Biomaterials*, vol. 34, no. 33, pp. 8061–8074, 2013.

[6] V. S. Polikov, P. A. Tresco, and W. M. Reichert, "Response of brain tissue to chronically implanted neural electrodes," *J. Neurosci. Methods*, vol. 148, no. 1, pp. 1–18, 2005.

[7] R. Chen, A. Canales, and P. Anikeeva, "Neural recording and modulation technologies," *Nature Rev. Mater.*, vol. 2, no. 2, 2017, Art. no. 16093.

[8] A. Campbell and C. Wu, "Chronically implanted intracranial electrodes: Tissue reaction and electrical changes," *Micromachines*, vol. 9, no. 9, 2018, Art. no. 430.

[9] D. A. Schwarz et al., "Chronic, wireless recordings of large-scale brain activity in freely moving rhesus monkeys," *Nature Methods*, vol. 11, no. 6, pp. 670–676, 2014.

[10] D. A. Borton, M. Yin, J. Aceros, and A. Nurmikko, "An implantable wireless neural interface for recording cortical circuit dynamics in moving primates," *J. Neural Eng.*, vol. 10, no. 2, 2013, Art. no. 026010.

[11] S. L. Bressler and V. Menon, "Large-scale brain networks in cognition: Emerging methods and principles," *Trends Cogn. Sci.*, vol. 14, no. 6, pp. 277–290, 2010.

[12] A. P. Alivisatos, M. Chun, G. M. Church, R. J. Greenspan, M. L. Roukes, and R. Yuste, "The brain activity map project and the challenge of functional connectomics," *Neuron*, vol. 74, no. 6, pp. 970–974, 2012.

[13] W. W. Seeley, R. K. Crawford, J. Zhou, B. L. Miller, and M. D. Greicius, "Neurodegenerative diseases target large-scale human brain networks," *Neuron*, vol. 62, no. 1, pp. 42–52, 2009.

[14] L. R. Hochberg et al., "Neuronal ensemble control of prosthetic devices by a human with tetraplegia," *Nature*, vol. 442, no. 7099, pp. 164–171, 2006.

[15] G. A. Tabot et al., "Restoring the sense of touch with a prosthetic hand through a brain interface," *Proc. Nat. Acad. Sci.*, vol. 110, pp. 18 279–18 284, 2013.

[16] S. Lee et al., "Battery-free neuromodulator for peripheral nerve direct stimulation," *Nano Energy*, vol. 50, pp. 148–158, 2018.

[17] D. T. Plachta et al., "Blood pressure control with selective vagal nerve stimulation and minimal side effects," *J. Neural Eng.*, vol. 11, no. 3, 2014, Art. no. 036011.

[18] P. B. Yoo, H. Liu, J. G. Hincapie, S. B. Ruble, J. J. Hamann, and W. M. Grill, "Modulation of heart rate by temporally patterned vagus nerve stimulation in the anesthetized dog," *Physiological Rep.*, vol. 4, no. 2, 2016, Art. no. e12689.

[19] H. Lyu, J. Wang, J.-H. La, J. M. Chung, and A. Babakhani, "An energy-efficient wirelessly powered millimeter-scale neurostimulator implant based on systematic codesign of an inductive loop antenna and a custom rectifier," *IEEE Trans. Biomed. Circuits Syst.*, vol. 12, no. 5, pp. 1131–1143, Oct. 2018.

[20] Y. Tanabe et al., "High-performance wireless powering for peripheral nerve neuromodulation systems," *PloS One*, vol. 12, no. 10, 2017, Art. no. e0186698.

[21] A. Wickens et al., "Magnetoelectric materials for miniature, wireless neural stimulation at therapeutic frequencies," *BioRxiv*, p. 461855, 2018.

[22] K. L. Montgomery et al., "Wirelessly powered, fully internal optogenetics for brain, spinal and peripheral circuits in mice," *Nature Methods*, vol. 12, no. 10, p. 969, 2015.

[23] J. Charthad et al., "A mm-sized wireless implantable device for electrical stimulation of peripheral nerves," *IEEE Trans. Biomed. Circuits Syst.*, vol. 12, no. 2, pp. 257–270, Apr. 2018.

[24] D. K. Piech et al., "Stimdust: A 2.2 mm3, precision wireless neural stimulator with ultrasonic power and communication," 2018, *arXiv:1807.07590*.

[25] S.-H. Cho, N. Xue, L. Cauller, W. Rosellini, and J.-B. Lee, "A su-8 based fully integrated biocompatible inductively powered wireless neurostimulator," *J. Microelectromech. Syst.*, vol. 22, no. 1, pp. 170–176, 2013.

[26] D. K. Freeman et al., "A sub-millimeter, inductively powered neural stimulator," *Frontiers Neurosci.*, vol. 11, p. 659, 2017.

[27] D. Szarowski et al., "Brain responses to micro-machined silicon devices," *Brain Res.*, vol. 983, no. 1-2, pp. 23–35, 2003.

[28] O. Veiseh et al., "Size-and shape-dependent foreign body immune response to materials implanted in rodents and non-human primates," *Nature Mater.*, vol. 14, no. 6, pp. 643–651, 2015.

[29] A. Khalifa et al., "The microbead: A highly miniaturized wirelessly powered implantable neural stimulating system," *IEEE Trans. Biomed. Circuits Syst.*, vol. 12, no. 3, pp. 521–531, Jun. 2018.

[30] A. Khalifa, J. Zhang, M. Leistner, and R. Etienne-Cummings, "A compact, low-power, fully analog implantable microstimulator," in *Proc. IEEE Int. Symp. Circuits Syst.*, 2016, pp. 2435–2438.

[31] A. S. Poon, S. O'Driscoll, and T. H. Meng, "Optimal frequency for wireless power transmission into dispersive tissue," *IEEE Trans. Antennas Propag.*, vol. 58, no. 5, pp. 1739–1750, May 2010.

[32] M. A. Adeeb, A. B. Islam, M. R. Haider, F. S. Tulip, M. N. Ericson, and S. K. Islam, "An inductive link-based wireless power transfer system for biomedical applications," *Active Passive Electron. Compon.*, vol. 2012, 2012, Art. no. 879294.

[33] M. Zargham and P. G. Gulak, "Fully integrated on-chip coil in $0.13\mu m$ CMOS for wireless power transfer through biological media," *IEEE Trans. Biomed. Circuits Syst.*, vol. 9, no. 2, pp. 259–271, Apr. 2015.

[34] W. Biederman et al., "A fully-integrated, miniaturized (0.125 mm^2) 10.5 μw wireless neural sensor," *IEEE J. Solid-State Circuits*, vol. 48, no. 4, pp. 960–970, 2013.

[35] P. Feng, T. G. Constandinou, P. Yeon, and M. Ghovanloo, "Millimeter-scale integrated and wirewound coils for powering implantable neural microsystems," in *Proc. Biomed. Circuits Syst. Conf.*, 2017, pp. 1–4.

[36] A. Khalifa, Y. Karimi, Y. Huang, M. Stanaćević, and R. Etienne-Cummings, "The challenges of designing an inductively coupled power link for ŀm-sized on-chip coils," in *Proc. IEEE Biomed. Circuits Syst. Conf.*, 2018, pp. 1–4.

[37] A. Khalifa, Y. Karimi, M. Stanaćević, and R. Etienne-Cummings, "Novel integration and packaging concepts of highly miniaturized inductively powered neural implants," in *Proc. 39th IEEE Eng. Med. Biol. Soc.*, pp. 234–237, 2017.

[38] R. Gerwig et al., "PEDOTCNT composite microelectrodes for recording and electrostimulation applications: Fabrication, morphology, and electrical properties," *Frontiers Neuroeng.*, vol. 5, p. 8, 2012.

[39] E. Castagnola et al., "Smaller, softer, lower-impedance electrodes for human neuroprosthesis: A pragmatic approach," *Frontiers Neuroeng.*, vol. 7, p. 8, 2014.

[40] Y. Karimi, A. Khalifa, W. Montlouis, M. Stanaćević, and R. Etienne-Cummings, "Coil array design for maximizing wireless power transfer to sub-mm sized implantable devices," in *Proc. IEEE Biomed. Circuits Syst. Conf.*, 2017, pp. 1–4.

[41] X. T. Cui and D. D. Zhou, "Poly (3, 4-ethylenedioxythiophene) for chronic neural stimulation," *IEEE Trans. Neural Syst. Rehabil. Eng.*, vol. 15, no. 4, pp. 502–508, Dec. 2007.

[42] Y. Liu et al., "Soft conductive micropillar electrode arrays for biologically relevant electrophysiological recording," *Proc. Nat. Acad. Sci.*, vol. 115, no. 46, pp. 11 718–11 723, 2018.

[43] X. Chen, W. G. Yeoh, Y. B. Choi, H. Li, and R. Singh, "A 2.45-Ghz near-field RFID system with passive on-chip antenna tags," *IEEE Trans. Microw. Theory Techn.*, vol. 56, no. 6, pp. 1397–1404, Jun. 2008.

[44] V. W. Leung et al., "A CMOS distributed sensor system for high-density wireless neural implants for brain-machine interfaces," in *Proc. IEEE 44th Eur. Solid State Circuits Conf.*, 2018, pp. 230–233.

[45] N.-C. Kuo, B. Zhao, and A. M. Niknejad, "Equation-based optimization for inductive power transfer to a miniature CMOS rectenna," *IEEE Trans. Microw. Theory Techn.*, vol. 66, no. 5, pp. 2393–2408, May 2018.

Adam Khalifa (S'12) received the B.S and M.Phil. degrees in electronic and computer engineering from the Hong Kong University of Science and Technology, Hong Kong, in 2011 and 2013, respectively, and the Ph.D. degree in electrical and computer engineering from Johns Hopkins University, Baltimore, MD, USA, in 2019. His research interests include low-power mixed-signal CMOS circuit design for neural interfaces, wireless power transfer systems, microfabricated electrodes, and packaging of implantable systems.
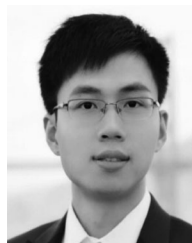
Yuxin Liu received the B.S and M.S. degrees from Nanyang Technological University, Singapore, and Stanford University, Stanford, CA, USA, respectively, and the Ph.D. degree in bioengineering from Stanford University in 2019. He developed stretchable bioelectronics and tissuelike neural interface in Prof. Z. Bao's group from 2014 to 2019.

Yasha Karimi (S'09) received the B.Sc degree from the University of Kashan, Kashan, Iran, in 2008, and the M.Sc. degree in electrical engineering from the Iran University of Science and Technology, Tehran, Iran, in 2011. He is currently working toward the Ph.D. degree at Stony Brook University, Stony Brook, NY, USA. His research interests include RF energy harvesting, ultralow-power analog and RF signal circuit design, and backscatter communication.

Qihong Wang received the M.D. degree from the Medical Center of Fudan University, Shanghai, China, in 1993. Prior to 2005, he served as a Pediatric Surgeon with the Children's Hospital of Fudan University. From 2006 to 2011, he received postdoctoral training with the Department of Surgery, Johns Hopkins University, Baltimore, MD, USA, where he joined the faculty in 2011 and the Department of Biomedical Engineering in 2015. He has more than ten years of experience with medical laboratory research and holds expertise in developing *in-vivo* animal models in mice, rats, and sheep. He has authored more than ten peer-reviewed articles.

Adebayo Eisape received the B.S. and M.S. degrees from the Johns Hopkins University, Baltimore, MD, USA, in 2012 and 2018, respectively, where he is currently working toward the Ph.D. degree at the Electrical and Computer Engineering Department. He is with the James West's group in the field of energy harvesting, and Sung-Hoon Kang's group in the field of piezoactive materials devices.

Milutin Stanaćević (S'00–M'05) received the B.S. degree in electrical engineering from the University of Belgrade, Belgrade, Serbia, in 1999. He received the M.S. and Ph.D. degrees in electrical and computer engineering from Johns Hopkins University, Baltimore, MD, USA, in 2001 and 2005, respectively. In 2005, he joined the faculty of the Department of Electrical and Computer Engineering, Stony Brook University, Stony Brook, NY, USA, where he is currently an Associate Professor. His research interests include mixed-signal VLSI circuit design for RF energy harvesting in implantable devices and tag networks, ultralow-power biomedical instrumentation and acoustic source separation.

Dr. Stanaćević is a recipient of the National Science Foundation CAREER award and IEEE Region 1 Technological Innovation Award. He was an Associate Editor of the IEEE Transactions on Biomedical Circuits and Systems and serves on several technical committees of the IEEE Circuits and Systems Society.

Nitish Thakor (F'94) received the B.S. degree in electrical engineering from the Indian Institute of Technology, Bombay, India, in 1974, the M.S. degree in biomedical engineering, and the Ph.D. degree in electrical and computer engineering from the University of Wisconsin, Madison, WI, USA, in 1978 and 1981, respectively. He is currently a Professor of biomedical engineering with Johns Hopkins University, Baltimore, MD, USA, as well as the Director of the Singapore Institute for Neurotechnology (SINAPSE), the National University of Singapore, Singapore. His technical expertise is in the field of neuroengineering, where he has pioneered many technologies for brain monitoring to prosthetic arms and neuroprosthesis. He is an author of more than 310 refereed journal papers (H Index 61), more than a dozen patents, and co-founder of three companies. He is currently an Editor-in-Chief of *Medical and Biological Engineering and Computing*, and was an Editor-in-Chief of the IEEE Transactions on Neural Systems and Rehabilitation Engineering from 2005 to 2011. He is a recipient of a Research Career Development Award from the National Institutes of Health and a Presidential Young Investigator Award from the National Science Foundation, and is a Fellow of the American Institute of Medical and Biological Engineering, Founding Fellow of the Biomedical Engineering Society, and Fellow of International Federation of Medical and Biological Engineering. He is a recipient of the award of Technical Excellence in Neuroengineering from the IEEE Engineering in Medicine and Biology Society, Distinguished Alumnus Award from the Indian Institute of Technology, Bombay, India, and a Centennial Medal from the University of Wisconsin School of Engineering.

Zhenan Bao received the Ph.D. degree in chemistry from The University of Chicago, Chicago, IL, USA, in 1995. She is currently a K.K. Lee Professor in chemical engineering, and with courtesy appointments in chemistry and material science and engineering. She has been the Department Chair of chemical engineering since 2018. She is a member of the National Academy of Engineering and National Academy of Inventors. She founded the Stanford Wearable Electronics Initiative (eWEAR) and is the current Faculty Director. She is also an affiliated faculty member of Precourt Institute, Woods Institute, ChEM-H, and Bio-X.

Ralph Etienne-Cummings (F'13) received the B.S. degree in physics from Lincoln University, Lincoln, PA, USA, in 1988, and the M.S.E.E. and Ph.D. degrees in electrical engineering from the University of Pennsylvania, Philadelphia, PA, USA, in 1991 and 1994, respectively. He is currently a Professor of electrical and computer engineering, and computer science with The Johns Hopkins University, Baltimore, MD, USA. He was the Founding Director of the Institute of Neuromorphic Engineering. He has authored more than 200 peer-reviewed articles and holds numerous patents. He has served as the Chairman of various IEEE Circuits and Systems (CAS) Technical Committees and was elected as a member of CAS Board of Governors. He also serves on numerous editorial boards. He is a recipient of the NSFs Career and Office of Naval Research Young Investigator Program Awards. He was a Visiting African Fellow at the University of Cape Town, Fulbright Fellowship Grantee, Eminent Visiting Scholar at the University of Western Sydney and has also received numerous publication awards, including the 2012 Most Outstanding Paper of the IEEE Transactions on Neural Systems and Rehabilitation Engineering. In addition, he was recently recognized as a Science Maker, an African American history archive.